Received: 26 April 2023 | Revised: 23 June 2023 | Accepted: 26 June 2023

DOI: 10.1049/rsn2.12432

IET Radar, Sonar & Navigation

The Institution of Engineering and Technology WILEY

ORIGINAL RESEARCH

# Statistical analysis of hypersonic glide vehicle radar cross section

Jonathan Pinto[1] | Neil L. Whyman[2] | Matthew A. Ritchie[3] | Hugh Griffiths[3]

[1]Electronic Systems, BAE Systems Digital Intelligence, Chelmsford, UK

[2]Ministry of Defence, Whitehall, UK

[3]Electronic and Electrical Engineering, University College London, London, UK

**Correspondence**

Jonathan Pinto, BAE Systems DI, West Hanningfield Rd, Great Baddow, Chelmsford CM2 8HN, UK.
Email: jon.pinto@baesystems.com

**Funding information**

BAE Systems, Grant/Award Number: T.OH.000017.01

**Abstract**

The capability to design, manufacture and test Hypersonic Glide Vehicles (HGVs) has been demonstrated by a number of nations, and they are increasingly forming part of military inventories, potentially offering capabilities highly unique to this technology. This article reports the simulated Monostatic Radar Cross Section of a generic HGV in five frequency ranges, HF, VHF, UHF, L, and S-bands associated with different radar types. Full spherical datasets of complex co- and cross-polar data are synthesised so that backscatter resulting from illumination by r.f./microwave energy of linear or circular polarisation can subsequently be computed from the raw dataset. Circular polarisation is commonly employed by ground-based Ballistic Missile Early Warning Systems and Space Object Surveillance and Identification radars to avoid polarisation mis-match losses resulting from ionospheric Faraday rotation effects. The data was generated using Ansys' Finite Element Solver at 10, 150 and 430 MHz, with the Geometric Optics/Physical Optics based SBR+ solver employed for 1.3 and 3 GHz data. All data was produced at below the Nyquist sampling interval relevant to the target's electrical size. These datasets were then imported into a Matlab routine which extracted data over limited angular ranges associated with the likely radar line-of-sight in particular scenarios, typically having a standard deviation of ±10° about the direction of flight, applying either a Gaussian or Uniform sampling distribution as part of a Monte Carlo analysis. These extracted data were then used to form histograms giving the probability of sampling particular RCS values. Probability density functions and cumulative distribution functions were then fitted, to aid in the representation of statistical target fluctuations for each band and angular sampling range. The HGV exists in either the 'Rayleigh', 'resonance' or 'optical' scattering regimes, depending on its relative electrical size. The results suggest that for this target shape at HF and VHF cases a simple Swerling 0 (fluctuation invariant) approximation is adequate in most instances, whilst a Gamma distribution may be applied for UHF band cases. At L and S-band a Beta distribution was found to provide a good fit to the available data.

**KEYWORDS**

missiles, radar cross-sections, radar theory, radionavigation

## 1 | INTRODUCTION

Hypersonic Glide Vehicles (HGVs) offer unique challenges, in terms of detection and tracking, for ground-based radars. This results from their potentially high radial velocity with respect to the radar, unpredictable flight profile, and low altitude (in the latter case relative to conventional Re-entry Vehicles (RVs) following a ballistic trajectory). In evaluating the effectiveness of new and existing radars in detecting/tracking these vehicles, a radar-range equation based model is invariably constructed. In these models, HGV target RCS fluctuations, and so corresponding variations in the amplitude of the voltage signal in the detector and, ultimately, the probability of detection ($P_d$) for a given probability of false alarm ($P_{fa}$) and signal to noise ratio

(SNR), are represented using one of the ubiquitously applied set of distributions postulated by Peter Swerling in 1954 [1]. That work was built upon prior analysis by Marcum, [2].

Radar range equation calculations used to determine useful parameters such a maximum detection range ($R_{max}$) or probability of track following the application of an *m from n pulse* track initialisation scheme in the radar post-processing, often, very reasonably, assume the Swerling III or IV cases for 'missile-like'vehicles [3, 4], including hypersonics. These are based on a Chi-squared distribution representing fluctuations from one dominant scatterer with a small number of additional smaller sources of return, either varying from scan-to-scan (Case III) or pulse-to-pulse (Case IV). However, although this may be reasonable for co-polar scattering from an HGV that is a few wavelengths in size 'flying' towards the radar (i.e. at boresight) [5], it may not be appropriate for the same target at other wavelengths ($\lambda$), look angles, or polarisations. This work therefore sought to examine the applicability of the Swerling distributions to a generic HGV geometry, as a function of these parameters, developing custom fluctuation models in the process. The effect of using these models on SNR can then be computed and the results employed as part of radar range equation based calculations.

## 2 | THE RCS MODELS

Hypersonic Glide Vehicles vary considerably in size depending upon their design requirements, particularly the size and mass of the payload. However, they must all fit within the diameter of their respective boost vehicles which is often a Medium, Intermediate Range, or Intercontinental Ballistic Missile (MRBM/IRBM/ICBM), examples of which are given in [6, 7]. These, in turn, are generally dictated by launch tube diameter if associated with a current platform. A geometry was constructed that was broadly representative of existing in-service systems [8, 9], and based loosely on a shape already widely reported in the public domain [10]. A maximum width consistent with existing and proposed ICBMs such as Russia's RS-18A 'Stilletto' and RS-28 'Sarmat' suggests a diameter of 3 m [11]. The image from ref. [10] is shown in Figure 1.

Given a vehicle diameter of 3 m, the remaining dimensions were estimated by photogrammetry to be:

- Length – 5.0 m
- Body height – 1.05 m
- Fin slant height – 0.41 m
- Fin length – 1.4 m
- Fin width – 0.03 m
- Base width (max) – 1.5 m
- Base length – 3.85 m
- Nose radius – 0.1 m

The resultant geometry, as represented in Ansys' Electronics Desktop (HFSS) is shown in Figure 2, Figures 3 and 4.

The vehicle was assumed to be a Perfect Electrical Conductor (PEC). This is likely to be a reasonable

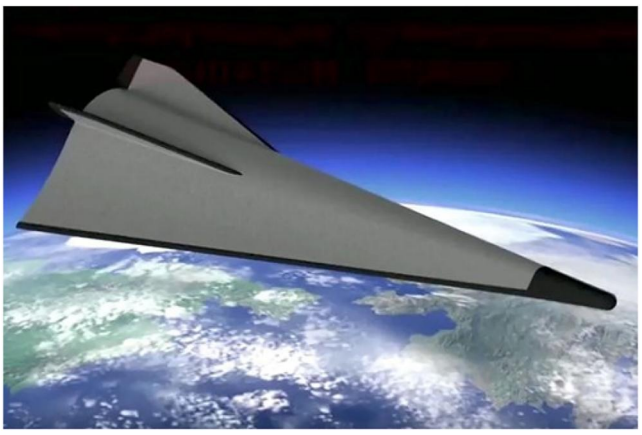

**FIGURE 1** Representation of generic boost-glide vehicle (hypersonic glide vehicle) from ref. [10].

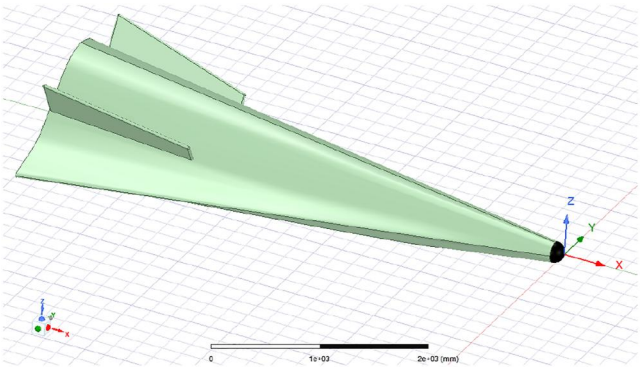

**FIGURE 2** Generic hypersonic glide vehicle representation in Ansys' HFSS, starboard side quarter view.

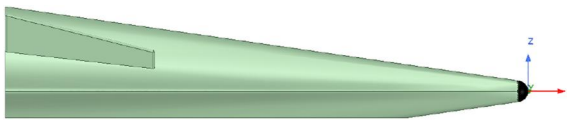

**FIGURE 3** Starboard broadside view.

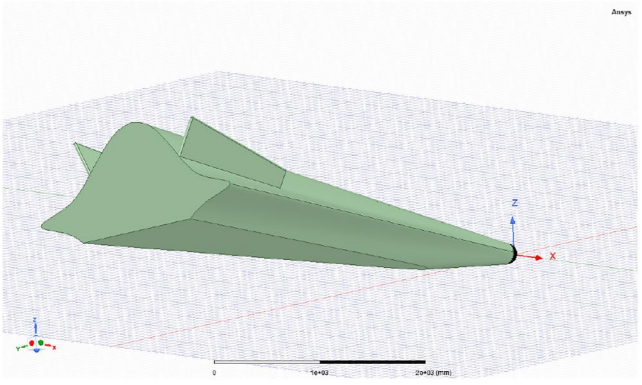

**FIGURE 4** Lower three quarter view of geometry in PO solver.

approximation for two reasons. Skin materials are generally similar to those used in more conventional RVs due to the need for thermal protection or ablation, typically consisting of carbon ceramic composites [12]. These have high conductivities at microwave frequencies leading to a surface voltage reflection co-efficient Γ, ≈−1 (the minus sign being present due to the 180° phase change which occurs when the incident EM wave travelling through a medium with a characteristic impedance of 377 Ω encounters a medium with a lower impedance).

At frequencies below 1 GHz, the assumption that the conductivity of carbon based composites is sufficiently high that it can be considered essentially infinite, can start to break down, being dependent on the fibre volume fraction and thickness of the composite. This leads to the possibility that the vehicle skin would exhibit a finite transmission loss, depending upon the thickness of the material in relation to the skin depth at a particular frequency. However, HGVs are generally well screened electrically in order to meet Nuclear Electromagnetic Pulse (NEMP) requirements so that the PEC approximation remains valid down to most practical radar operating frequencies, [13, 14].

Under certain circumstances, when operating endo-atmospherically (i.e. at an altitude below the Karman Line of around 100 km), it is possible that plasma effects, from aerodynamic heating of the air passing over the body, may have an impact on the overall RCS. Work undertaken as part of a previous study using a plasma model, [15], suggests that the plasma and collision frequencies result in an ionised region with a dispersive (frequency dependent) conductivity that has the potential to interact with the incident EM wave at HF, VHF and low UHF frequencies, but can be neglected at L-band and above [16]. This effect is not included in the HF, VHF and UHF data presented here because reliable data required for the model is not yet available. Results subsequently presented at these frequencies are therefore only relevant when the HGV is in the exo-atmospheric phases of flight.

In addition, at HF frequencies, when the vehicle is present at altitudes corresponding to the D, E, F1, F2 layers of the ionosphere, typically 50–400 km, its transit may cause the localised electron density of the plasma to vary, resulting in additional backscatter. It could therefore be argued that this effect is also part of the vehicle signature and would need to be accounted for in RRE calculations.

The Ansys' HFSS (2022R1) Shooting Bouncing Ray+ (SBR+) Geometric Optics/Physical Optics solver was used to simulate the backscatter from the geometry at UHF, L, and S-band frequencies (430 MHz, 1.3 GHz, and 3 GHz respectively), since the target is of reasonable electrical size in these instances. As such, contributions from second order scattering effects that are not always well represented by 'asymptotic' techniques are unlikely to contribute significantly to the overall scattered field, [17]. In any event, SBR+ includes diffraction effects via the Physical Theory of Diffraction, multiple bounces/shadowing via the Uniform Theory of Diffraction, and additionally creeping waves. The 'full-wave' Finite Element (FE) solver was used for the HF (10 MHz) and VHF (150 MHz) simulations, where the geometry was electrically small at some viewing angles.

The FE tetrahedral volume mesh used for HF simulations is shown, as a surface at the vacuum/body interface, in Figure 5. The boundary box had dimensions of 30 m by 20 m by 20 m, being a compromise between accuracy and solver run-time/memory requirements. At 10 MHz the mesh need only been extremely coarse with individual body elements being ≈900 mm (≈λ/30), with greater refinement around smaller features. The corresponding VHF (150 MHz) mesh projection is shown with the 8 m by 4 m, by 3 m boundary box in Figure 6. Individual mesh elements are around 200 mm ($\lambda/10$) in side-length.

The SBR+ surface mesh at 1.3 GHz is shown Figure 7 by way of example.

Note that the vehicle representation is shown with an $x$-oriented long axis, using a conventional right-handed

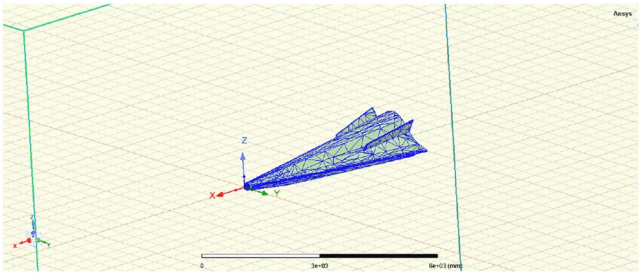

**FIGURE 5** Tetrahedral volume mesh shown at body interface as a surface in HFSS' finite element solver, 10 MHz.

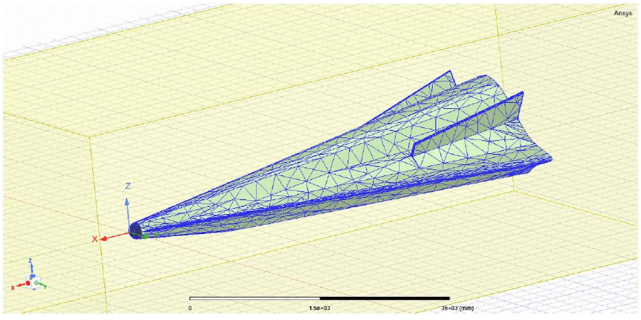

**FIGURE 6** HFSS' finite element mesh projection at 150 MHz.

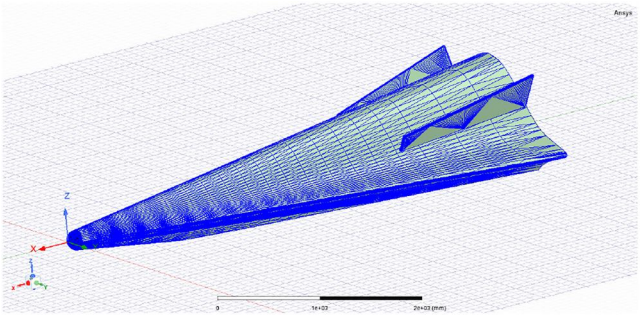

**FIGURE 7** Triangular surface mesh used in SBR+, 1.3 GHz.

co-ordinate system. In subsequent discussions regarding the datasets, $\theta$ is thus defined as going from the $z$-axis at zenith, in the direction of the $x$-axis, pointing forwards, whilst $\varphi$ extends from $x$ to $y$ (towards the port side) in the conventional manner.

Validation of the software was not undertaken explicitly in this instance, since a previous exercise had been undertaken using a different geometry, obtaining good results between this, scale model measurements, the in-house FDTD solver 'AGATE' and the PO based tool 'MITRE' [18].

## 3 | RUNNING THE SOLVERS AND EXTRACTING RESULTS

At 10 MHz, using Ansys' FE solver, the model required around 5 min to run on 32 Intel Xeon cores using around 1 GB of RAM, a single run providing results for one illumination polarisation. At 150 MHz the run-time increased to 2 hours. Total disk space used was substantial at around 100 GB. The SBR+ solver ran in around 2 h at 3 GHz, requiring approximately 1 GB of RAM and <2 GB of hard disk space, UHF and L-band results taking correspondingly less time.

The ($\theta$,$\varphi$) step was set according to the Nyquist angular sampling interval, in order to avoid phase ambiguities (see Table 1). The interval in angle for RCS (2 way) sampling can be calculated by first assuming that the target is enclosed in a sphere whose radius, $a$, corresponds to the maximum extent of the target in any given direction, Figure 8, [19]. The number of points necessary around a circle of circumference $2\pi a$ is given in Equation (1).

$$N_{\text{Nyquist}} = \frac{2\pi a}{\frac{\lambda}{2}} = \frac{4\pi a}{\lambda} \tag{1}$$

If the diameter, $d = 2a$ then,

$$N_{\text{Nyquist}} = \frac{2\pi d}{\lambda} \tag{2}$$

Now, the angular increment, in radians, is thus,

$$\theta_{\text{Nyquist}} = \frac{2\pi}{N_{\text{Nyquist}}} = \frac{\lambda}{d} \tag{3}$$

This is true for single path measurements. However, for RCS or other 'round trip' scattering problems, the distance travelled is doubled and the angular increment must be halved giving the result in Equation (4).

$$\theta_{\text{Nyquist}} = \frac{\lambda}{2d} = \frac{\lambda}{4a} \tag{4}$$

Halving the result to account for the round-trip path is essentially the same as stipulating a one-way path with a sampling interval of $\lambda/4$.

The increments subsequently used, with the Nyquist sampling angle, are given in Table 1 for each frequency band. The sampling angles were generally sub-Nyquist due to the need to ensure adequately sized datasets for subsequent statistical analysis when RCS values only from a limited angular range (i.e. selection of 'look' angles) might be taken from the full datasets.

The resultant RCS was obtained over $-180° \leq \varphi \leq 180°$ and $0° \leq \theta \leq 180°$. Changes in $\theta$ are essentially cuts akin to the segments of an orange moving from zenith (above the vehicle to the underside. A $\theta = 90°$ (varying $\varphi$) cut thus represents a range of azimuth angles around the vehicle at zero elevation in a counter-clockwise direction, whilst a $\varphi = 0°$ cut moves vertically around the vehicle body (in the $xz$-plane; for co-ordinate system see figures).

Complex RCS data was exported from the solvers and subsequently post-processed in a *Matlab* script so that either linear or circularly polarised (CP) RCS could subsequently be synthesised from the 8 files generated for each run [Re(Vθ), Im (Vθ), Re(Vφ), Im(Vφ), Re(Hθ), Im(Hθ), Re(Hφ), Im(Hφ)], these representing the co- and cross-polar components of the scattered field.

**TABLE 1** Angular sampling versus frequency.

| Band | Wavelength (m) | Nyquist (°) | Actual (°) |
|---|---|---|---|
| HF | 30 | 172 | 5 |
| VHF | 2 | 11.5 | 5 |
| UHF | 0.7 | 4.0 | 1 |
| L | 0.23 | 1.3 | 0.5 |
| S | 0.1 | 0.57 | 0.25 |

## 4 | LINEAR CO-POLAR RCS DATA

Simple azimuth cuts are shown for HH and VV polarisations in each of the five bands in Figure 9 through Figure 18, with a representation of the vehicle superimposed.

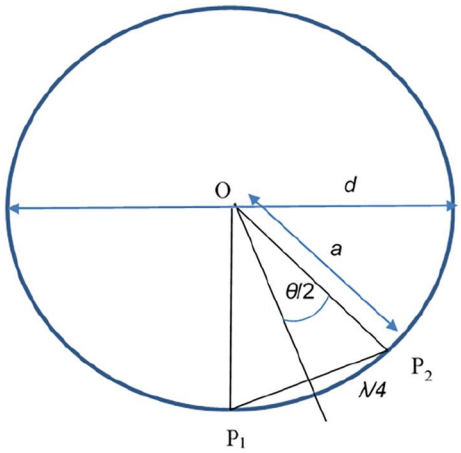


**FIGURE 8** Representation of two points on the circumference of a circle containing the target, separated by ≤λ/2.

At 10 MHz, Figures 9 and 10, since the target is always ≤λ/6 in electrical size, scattering can generally be regarded as Rayleigh in nature, although from the results, it is clearly not a point scatterer. The scattering lobes are however extremely broad but HH and VV Tx and Rx can be seen to result in patterns with the same general shape but with features of differing angular extents and levels. The azimuth cut pattern is dominated by four main lobes at the cardinal points. Subsequent analysis suggested that the $\varphi = 0°$ (forward) lobe is largely the result of the impedance mis-match which results from the incident EM wave encountering the sharp discontinuity at the rear of the fuselage, not the specular return from the hemispherical nose (which is electrically too small to result in significant backscatter). Removing this, by changing the aft geometry and re-running, substantially reduces the lobe's magnitude. The $\varphi = 180°$ (rear-facing) lobe also results from the impedance mis-match presented by the aft-end of the fuselage. At these wavelengths the width of this is only ≈λ/10 and backscatter is not therefore truly specular. The lobes at $\varphi = \pm 90°$ are a consequence of the dihedrals that exist between the vehicle body and the aft control surfaces. Their removal causes these lobes to largely disappear. In subsequent 3D scattering plots it can be seen that these dihedrals, together with flat surfaces on the underside, result in broadside scatter over a large angular range in elevation. The resultant combination creates a lobe that extends fully around the vehicle over all $\theta$ at $\varphi = \pm 90°$ (i.e. in the $yz$-plane).

At VHF (150MHz) frequencies, Figures 11 and 12, target dimensions are of the same order as a wavelength. It is in this 'resonance' region that one would expect the largest differences between polarisations, as different parts of the structure are excited in each case.

Compared with the HF case, additional features can be seen as particular vehicle dimensions become resonant at different aspect angles. The UHF band linear co-polar azimuth cuts are shown in Figures 13 and 14. The boresight RCS is much reduced as diffraction from the discontinuity at the end of the fuselage is less than for the previous longer wavelength cases, whilst the specular return from the nose remains small. Separate spikes can now start to be resolved from the control

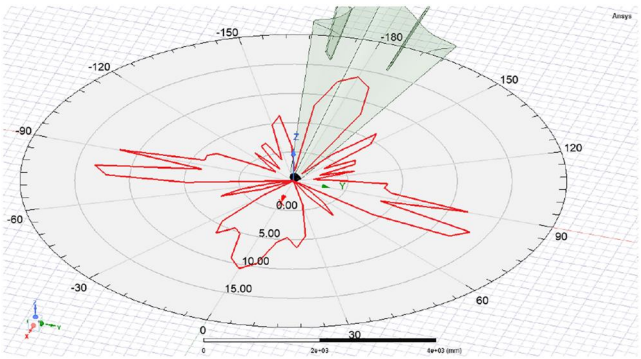


**FIGURE 11** HH pol'n, azimuth cut, 150 MHz.

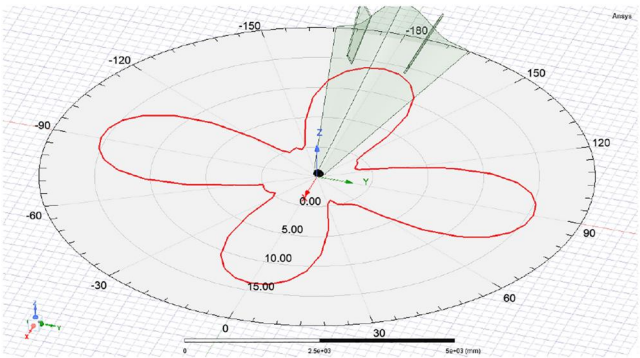


**FIGURE 9** HH pol'n, azimuth cut at 0° elevation, 10 MHz.

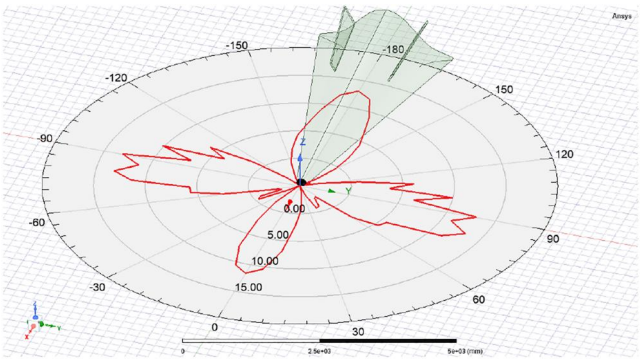


**FIGURE 12** VV pol'n, azimuth cut, 150 MHz.

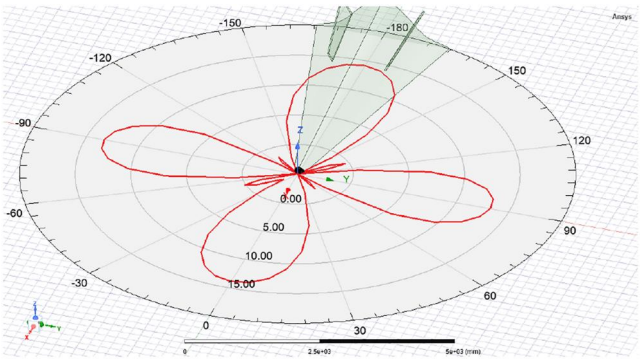


**FIGURE 10** VV pol'n, azimuth cut at 0° elevation, 10 MHz.

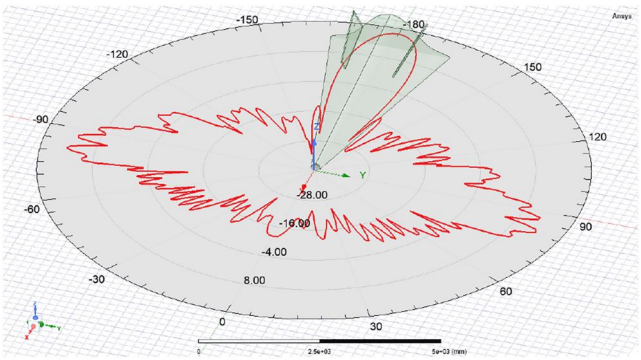


**FIGURE 13** HH pol'n, azimuth cut, 430 MHz.

surface-fuselage dihedral and the edge of the flat base (see Figure 4) near $\varphi = \pm 79°$, particularly in HH polarisation, where the H-field being perpendicular to the underbody drives a surface travelling wave.

Results for L-band (1.3 GHz, 23 cm) are shown in Figures 15 and 16. Here, the target is in the optical scattering regime with most dimensions being electrically large. The results for the two polarisations become increasingly similar as the electrical size of the target increases.

The lobes become narrower as the electrical size of the specular scatterers, in particular, become larger.

The final co-polar results for S-band are shown in Figures 17 and 18. Only the negative hemisphere data were predicted at 3 GHz since the 0.25° angular increment resulted in a dataset of 519,841 points per polarisation. Larger arrays were found to be difficult to handle within HFSS. Symmetry was invoked in the *Matlab* routine to synthesise a full spherical dataset in post-processing.

The Matlab code additionally included a routine written to represent the full datasets on a 3D plot by conversion of the ($\theta$, $\varphi$) co-ordinates to Cartesian data points and subsequent plotting of those ($x$,$y$,$z$) values using the *surf* command. These illustrate the variation in the nature of the scattered field in the different bands. Only the HH polarisation data is presented, as the VV (and other cases) support the same general conclusions.

The polar plot for the HF-band case is shown in Figure 19. The target's long axis is oriented along the $x$-direction, with the planar underside (see Figure 4) being parallel to the xy-plane.

As would be expected, as the target becomes electrically larger, the general RCS values increase. At 10 MHz, Figure 19, scattering is dominated by broad lobes along the principal axes, associated with impedance discontinuities in the free-space transmission line. These are mostly due to the planar aft fuselage, 'fins', and, when viewed from zenith and underneath, the predominantly flat aspect of the vehicle itself.

At 150 MHz, Figure 20, the dihedrals associated with bounces between the fins and the fuselage provide reflections over a broad range of elevation angles at $\varphi \approx \pm 90°$. These join with specular reflections from the top and fin-inside-edges, which form further dihedrals, and the flat base of the fuselage,

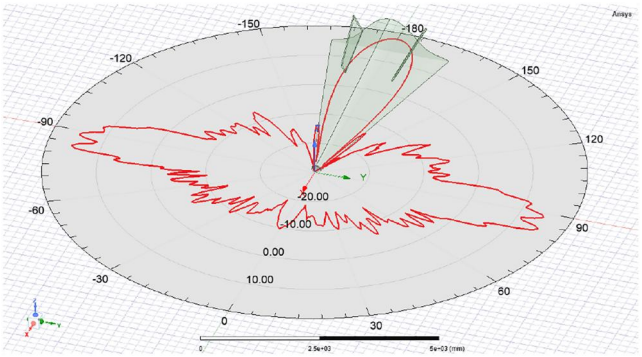


**FIGURE 14** VV pol'n, azimuth cut, 430 MHz.

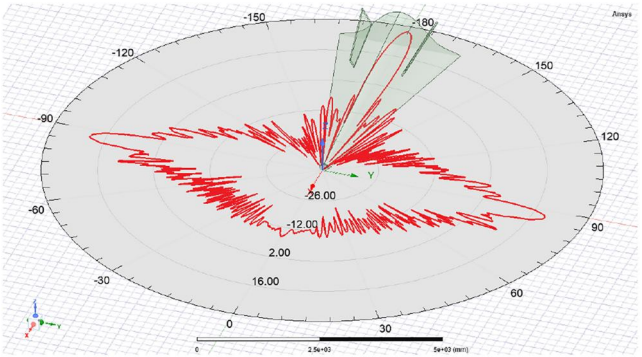


**FIGURE 15** HH pol'n, azimuth cut, 1.3 GHz.

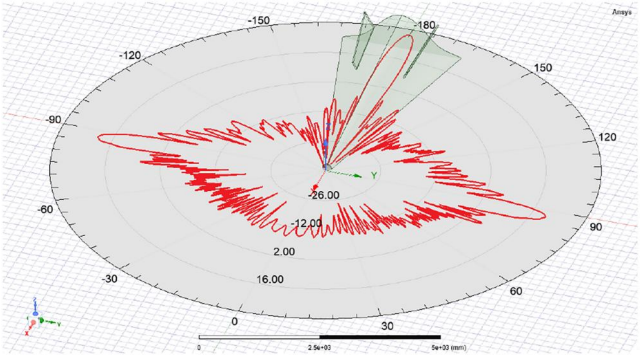


**FIGURE 16** VV pol'n, azimuth cut, 1.3 GHz.

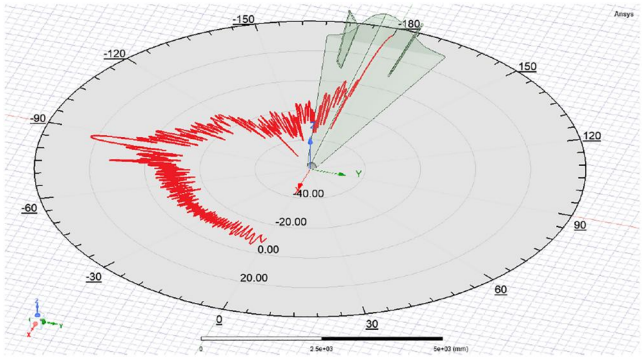


**FIGURE 17** HH pol'n, azimuth cut, 3 GHz.

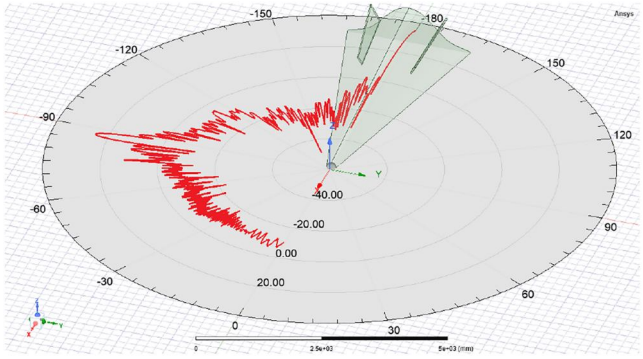


**FIGURE 18** VV pol'n, azimuth cut, 3 GHz.

to form a continuous 'ring' of high monostatic RCS in the yz-plane.

Greater detail exists in the scattered field as the frequency increases, as can be seen by comparing Figure 19 with Figure 20 and subsequent images. The angular extent of scattering lobes becomes progressively smaller as additional resolution becomes available with increasing frequency, as can be seen in the case of the UHF, L, and S-band results shown in Figures 21–23.

At microwave frequencies, full 3D plots of monostatic RCS give a valuable insight into the likely scattering mechanisms and positions of the scatterers which dominate the overall RCS for most aspect angles. However, this information can come at the cost of significant run-times and the need to manipulate large datasets if under-sampling is to be avoided.

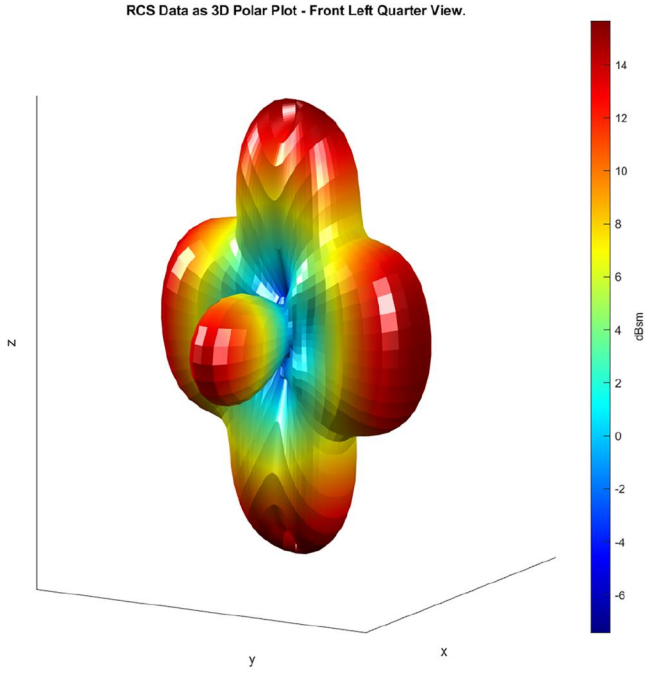


**FIGURE 19** 3D polar plot of RCS in HF-band, HH pol'n.

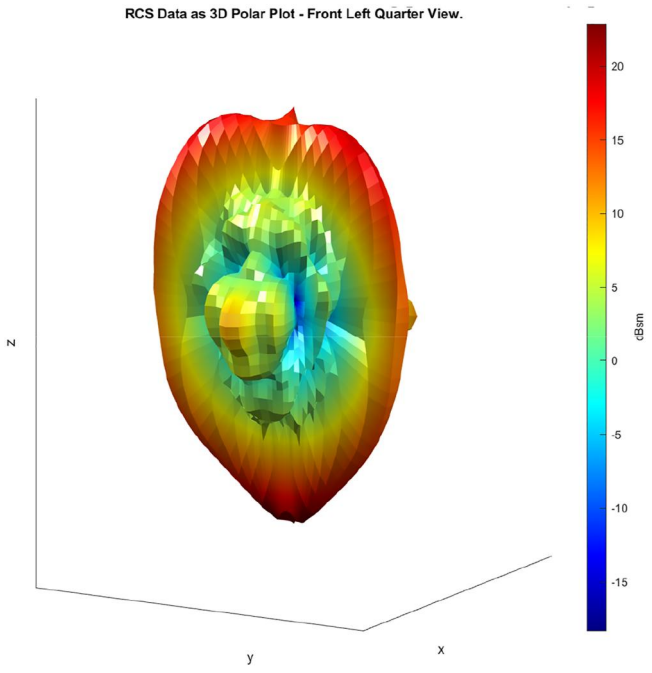


**FIGURE 20** 3D polar plot of RCS in VHF-band, HH pol'n.

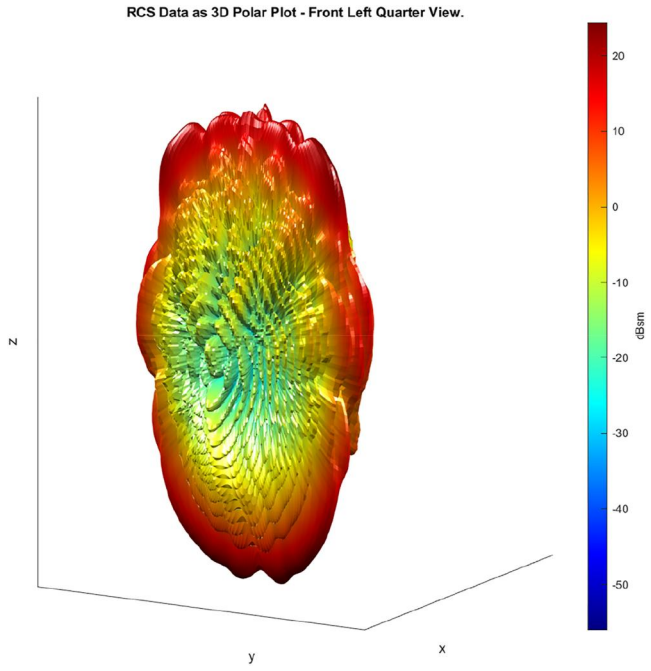


**FIGURE 21** 3D polar plot of RCS in UHF-band, HH pol'n.

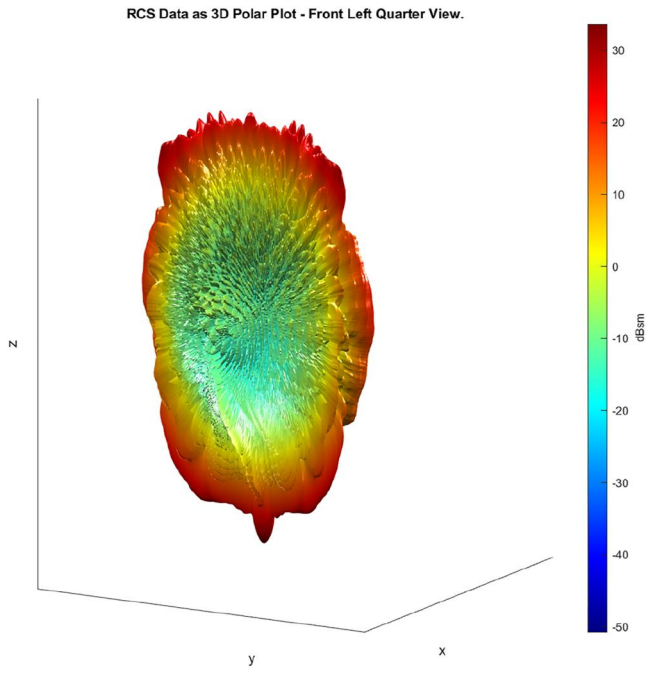


**FIGURE 22** 3D polar plot of RCS in L-band, HH pol'n.

Although the technique is not shown explicitly in this paper, the removal of features from the CAD geometry, followed by re-prediction of the RCS can be a valuable aid in identification of particular scatterers.

## 5 | CIRCULAR POLARISATION RCS SYNTHESIS

The scattered field from a target illuminated by a CP incident wave is not necessarily the same as for the linear case. In instances where the target exhibits rotational (radial) symmetry when viewed from a particular radar line of sight then the CP and linear RCS values coincide. For all other situations, the scattered fields will differ, leading to differences in the RCS as a function of polarisation.

Randrianandrasana et al, [20], give a mathematical description of incident wave polarisation based on the book by Ruck, [21], and the resulting target scattering matrix, [S], formulae for linear and circular cases. The linear case is given in Equation (5), relating the horizontal and vertical components of the scattered E-fields (superscript, '*s*') to the incident ones (superscript '*i*').

$$\begin{bmatrix} E_H^s \\ E_V^s \end{bmatrix} = \begin{pmatrix} s_{HH} & s_{HV} \\ s_{VH} & s_{VV} \end{pmatrix} \begin{bmatrix} E_H^i \\ E_V^i \end{bmatrix} \tag{5}$$

$S_{xx}$ are the scattering parameters within the scattering matrix and are complex voltage ratios. Similar to (5), the right and left hand circular scattered fields are related to the incident fields as per Equation (6).

$$\begin{bmatrix} E_R^s \\ E_L^s \end{bmatrix} = \begin{pmatrix} s_{RR} & s_{RL} \\ s_{LR} & s_{LL} \end{pmatrix} \begin{bmatrix} E_R^i \\ E_L^i \end{bmatrix} \tag{6}$$

This leads to equations for the CP co- and cross-polar scattered fields in terms of the linear components, Equations (7)–(10), as outlined in ref. [20].

$$S_{RR} = \frac{-S_{V\theta} + S_{H\phi} - (S_{H\theta} + S_{V\phi})i}{2} \tag{7}$$

$$S_{RL} = \frac{S_{V\theta} + S_{H\phi} + (S_{H\theta} - S_{V\phi})i}{2} \tag{8}$$

$$S_{LR} = \frac{S_{V\theta} + S_{H\phi} - (S_{H\theta} - S_{V\phi})i}{2} \tag{9}$$

$$S_{LL} = \frac{-S_{V\theta} + S_{H\phi} + (S_{H\theta} + S_{V\phi})i}{2} \tag{10}$$

The RCS magnitude can then be extracted by taking the $20\log_{10}(|S_{xx}|)$ in each case. By way of example, the RR scattered field is presented for the target in the UHF band, Figure 24. The result can be compared against linear HH co-polar result of Figure 21. Away from the *x*-axis, there is little radial symmetry and the results are therefore somewhat different.

Note that a Ballistic Missile Early Warning Systems radar transmitting RHCP will illuminate the target which will change the sense of polarisation as the energy is reflected so that RH will predominantly become LH. However, although LH returns towards the monostatic radar, this definition is in the

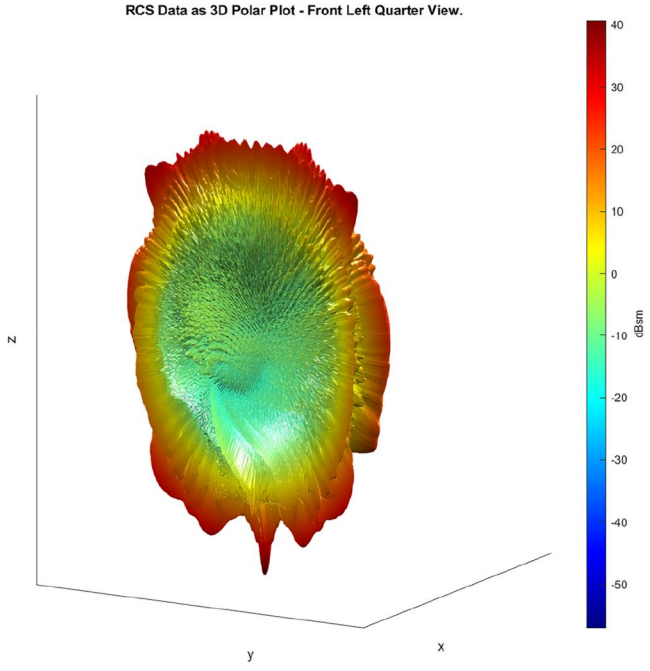


**FIGURE 23** 3D polar plot of RCS in S-band, HH pol'n.

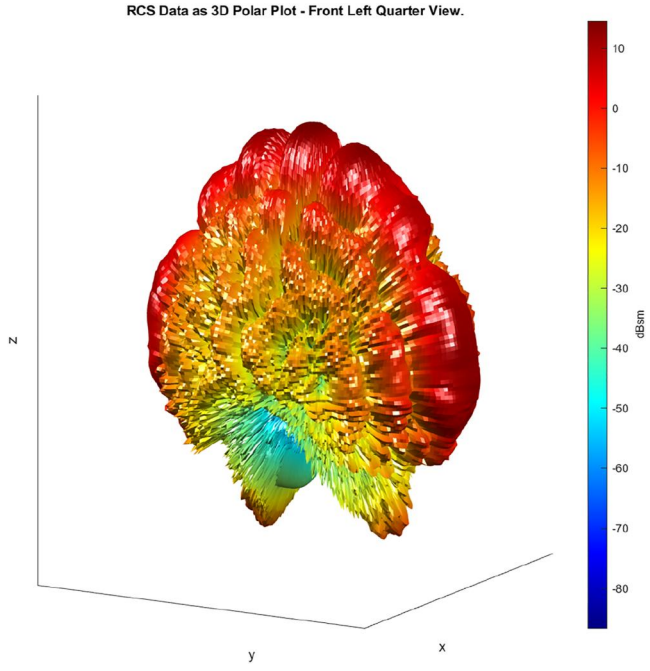


**FIGURE 24** 3D polar plot of RCS in UHF-band, RHCP pol'n.

direction of propagation. When viewed from behind the array face, the LH becomes RH once again. Consequently, an antenna element transmitting RHCP radiation will also accept RHCP radiation with little polarisation mis-match loss if a single bounce has taken place on the target surface. RHCP that has undergone an even number of bounces, such as via ground induced multipath will be largely rejected.

## 6 | REPRESENTING TARGET FLUCTUATION

Swerling's Rand Corporation paper [1] on target fluctuation statistics postulated that RCS target variations for most typical air vehicle types could generally be adequately described by either a negative exponential distribution of the form given in Equation (11), Swerling (I/II) or a distribution given by Equation (12), constituting Swerling cases (III/IV). I and III assume that the target varies its echoing area only from scan to scan (which for modern phased arrays can be interpreted as being over the radar's dwell period). Cases II and IV apply when the fluctuation occurs rapidly to the extent that it varies from pulse-to-pulse. The additional case, whereby the target RCS remains invariant over time, which is predominantly dealt with in Marcum's paper [2], is generally referred to as Swerling 0.

$$f(\sigma,\overline{\sigma}) = \frac{1}{\overline{\sigma}} e^{\frac{-\sigma}{\overline{\sigma}}} \tag{11}$$

$$f(\sigma,\overline{\sigma}) = \frac{4\sigma}{\overline{\sigma}^2} e^{\frac{-2\sigma}{\overline{\sigma}}} \tag{12}$$

In many texts on statistics, $\sigma$ is used to represent the mean. Throughout this paper, $\sigma$ represents the RCS sample value, whilst $\overline{\sigma}$ describes the former. It also represents the scale parameter of the Probability density function (PDF) in both instances.

One point of common confusion, clarified in Skolnik, [22], is that targets which exhibit RCS fluctuations (in the form of received *power*) that can be described by the negative exponential of Equation (11), are often referred to as "*Rayleigh targets*", because those power fluctuations lead to *voltage* changes in the detector which are best described statistically by a Rayleigh PDF (PDF). Swerling's case III and IV of Equation (12) is also sometimes incorrectly referred to as Rayleigh but is actually Chi-squared, itself a special case of the Gamma distribution. At first glance the distributions can appear similar, Figure 25.

Generally, unless the HGV target is either tumbling, or manoeuvring very rapidly, it is inappropriate to use the full spherical datasets to form distributions to represent fluctuations. Consequently a Monte-Carlo analysis option was written into the *Matlab* script which extracts data over a limit range of ($\theta$,$\varphi$) radar-line-of-sight values. Two modules were developed to attempt to cover most general cases associated with typical trajectories.

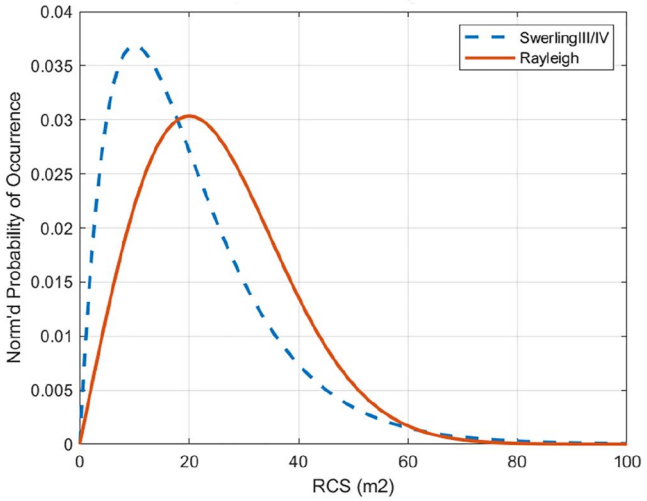


**FIGURE 25** Comparison of Swerling (III/IV) Chi-squared power case against a Rayleigh Probability density function (PDF).

In the first, the user specifies a nominal 'look angle' followed by a standard deviation in $\theta$ and $\varphi$. The first step of the Monte-Carlo analysis then proceeds by assigning a normal distribution centred on the $\varphi$ (azimuth) angle selected. The corresponding cumulative distribution function (CDF) (CDF) is calculated and this is used to pick 1000 azimuth angle points who's 'probability of pick' is then weighted according to the normal distribution assigned. The selection is quantised according to the Nyquist sampling interval (or smaller) chosen earlier. This then leads to a 1000 element vector of randomly picked values, with Gaussian weighting about the 'nominal' value. For example, this situation might occur when the HGV were travelling directly towards a ground based radar as the target, or some other known point. In this case, the nominal angle presented by the target to the radar is thus also known, and the probability of sampling the RCS at other angles decreases with increasing positive or negative deviation from the nominal one. This exercise was repeated in $\theta$ (elevation) so that angles picked in both azimuth and elevation have probabilities dictated by normal distributions centred on the nominal ($\theta$,$\varphi$) co-ordinate chosen. This leads to two Gaussian like histograms of sampled angle versus occurrence. The PDF, CDF, and resultant Gaussian-like histograms for $\theta$ and $\varphi$ are shown for the UHF, HH pol'n case with boresight (90°,0°) as the nominal angular value and a standard deviation (s.d.) of $\theta = \varphi = 10°$, by way of example in Figures 26–29. The application of a normal distribution means that 99.7% of sampled angles lie within 3 s.d. of the mean (i.e. within ±30°).

These 1000 × 1000 angle samples are then used to 'look-up' the corresponding RCS values, resulting in a histogram of probability of occurrence versus RCS magnitude for the overall dataset of 1 million samples.

A second routine, which assumed all angles about a nominal value over a given interval were equally likely to be selected (i.e. with a Uniform distribution applied in $\theta$ and $\varphi$) was written. This is not reported further here, since the Gaussian approach is more generally applicable, but it is

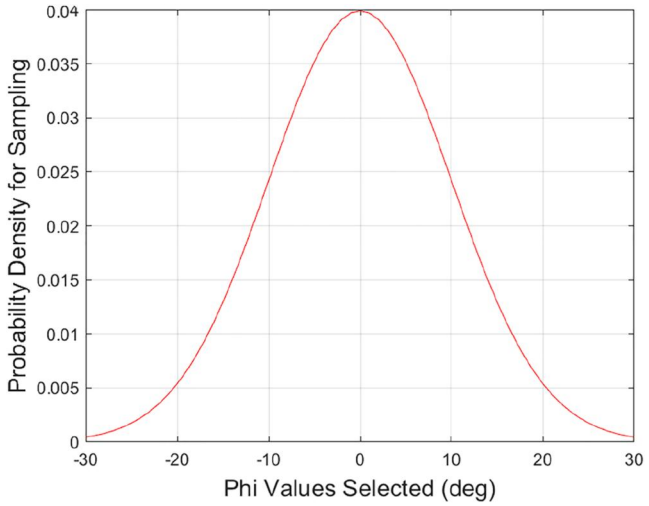


**FIGURE 26** Gaussian pdf sampling for $\varphi$ with s.d. = 10°.

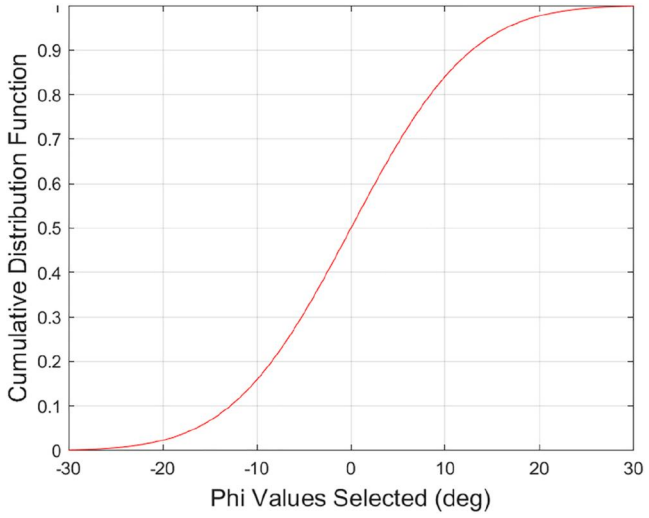


**FIGURE 27** Corresponding cdf used for value picking.

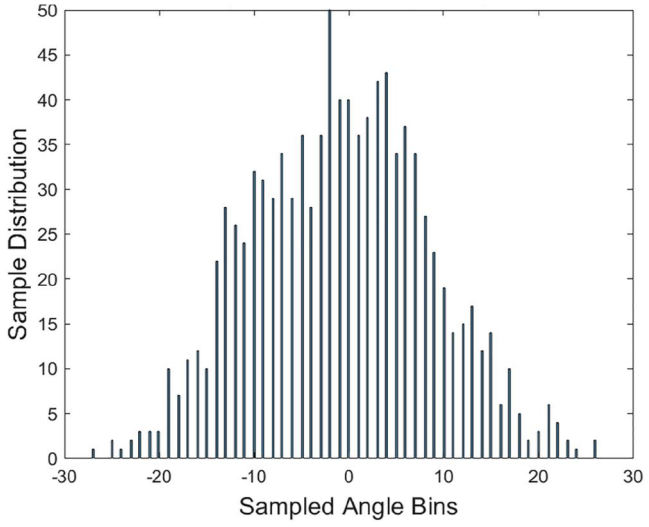


**FIGURE 28** Histogram of picked $\varphi$ (azimuth) angles.

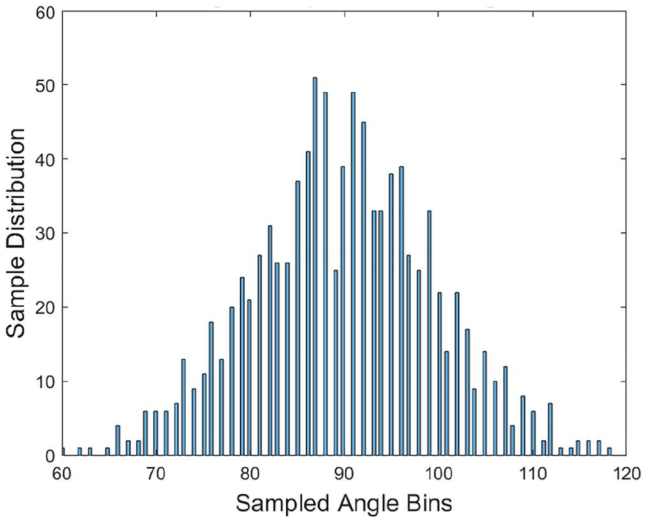


**FIGURE 29** Histogram of picked $\theta$ (elevation) angles.

important to point out that the Gaussian angular variation is not applicable in all instances. This approach ultimately leads to PDFs which are each themselves a function of $\theta$ and $\varphi$.

## 7 | RESULTANT FLUCTUATION MODELS

The preceding Monte-Carlo analysis gave rise to a series of RCS histograms, varying with frequency, look angle, distribution selected for angular sampling, range of angular values sampled, and polarisation. The effect of frequency band variation for a single case, that of HH pol'n, normal distributions, boresight nominal angle and a sampling extent of 10° standard deviation (i.e.99.7% of sampled data lying within $|\theta|, |\varphi| \leq 30°$ are described subsequently. The HF case is somewhat anomalous as surface and skywave Over The Horizon Radars may 'dwell' in a target region for long periods to improve SNR. In the terminal phase, HGVs may therefore manoeuvre (both in angle presented and absolute position) considerably during a single dwell. In the HF-band, an angular standard deviation of 10° is perhaps therefore only representative if the target is not in a manoeuvring phase of flight. However, by keeping this parameter constant, it permits comparison of the effect of differing frequencies, without additional complication. Equally, an illumination angle corresponding to boresight, although quite feasible for an HF surface wave radar is highly improbable for a skywave system.

Figure 30 shows an HF band histogram. The distribution is not well served by the Swerling I and Swerling III type distributions, both in terms of the histogram shape and because it is discontinuous (the number of bins was held constant at 100 for all cases, for consistency).

Re-sampling of the same HF dataset by repeating the Monte-Carlo analysis resulted in histograms which appeared almost identical to that of Figure 30, as shown in Figure 31, suggesting that the extent of sampling is sufficient to be give a

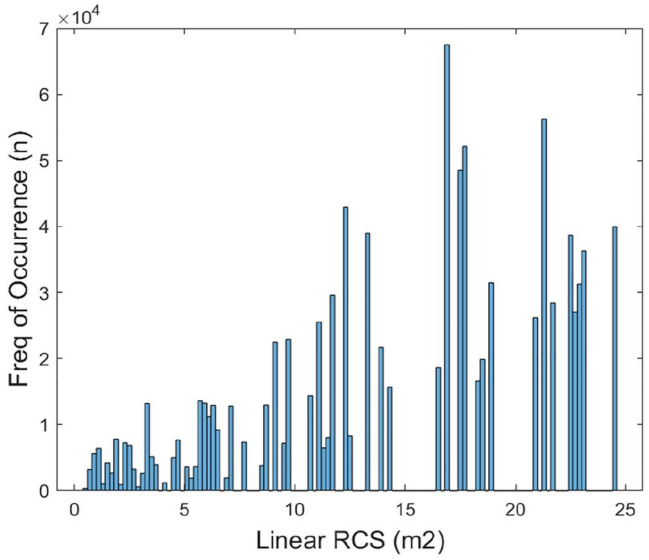


**FIGURE 30** 10MHz RCS histogram, HH, broadside, s.d. = 10°.

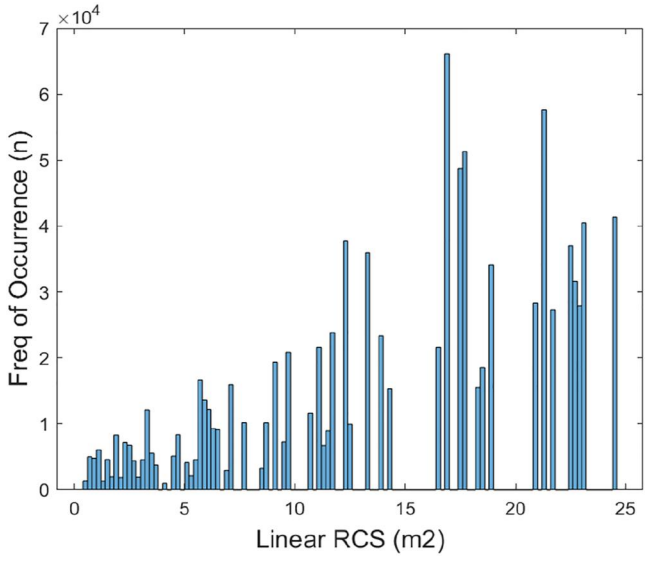


**FIGURE 31** Re-sampled 10MHz data histogram.

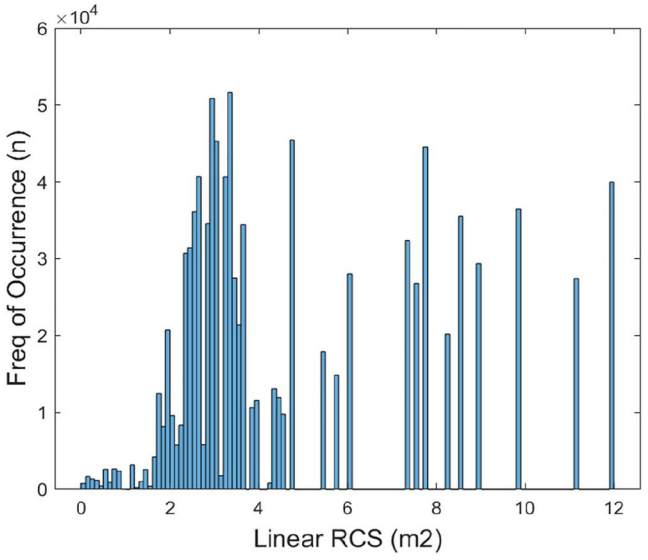


**FIGURE 32** 150MHz RCS distribution, HH pol'n, broadside, s.d. = 10°.

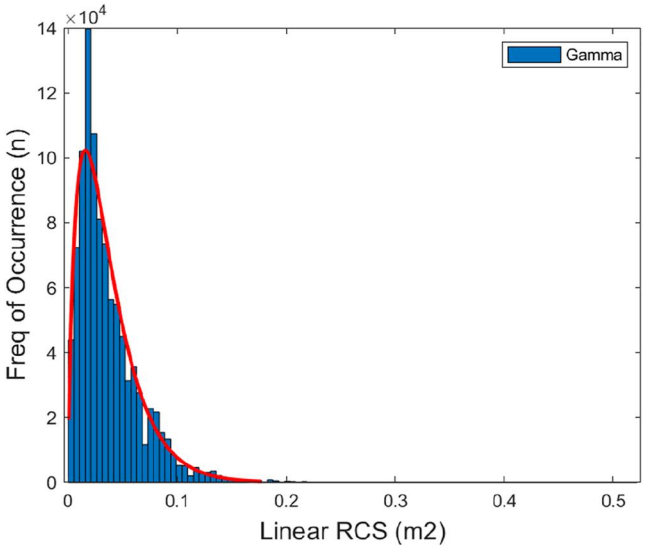


**FIGURE 33** 430 MHz RCS distribution, HH pol'n, broadside, s.d. = 10°, Gamma dist'n applied.

stable output. Figure 32 shows the VHF case. In both HF and VHF cases the datasets are not particularly well served by typical continuous PDFs, for the polarisation, nominal 'look-angle', Gaussian sampling approach, and s.d. chosen.

The UHF case is shown in Figure 33, and was best fitted by a Gamma distribution. The L-band case is shown in Figure 34. Although the fit is not quite as good as that of the UHF case, the data were found to be best represented by a Beta function.

The 3GHz data were also found to be best-represented by a Beta PDF, as shown in Figure 35.

By way of example, the CDF (CDF) was evaluated for the Swerling I/II, III/IV, and Beta distributions, as applied to the S-band dataset. The results are shown in Figure 36. The RMS error for the Beta derived CDF is lower than for the other cases, suggesting that it constitutes a better fit. Swerling III/IV is arguably a better representation than the negative exponential of Swerling I/II.

## 8 | CONCLUSION

Sufficient computing power now exists, together with advances in EM code development to allow full 3D scattering patterns, at or below the Nyquist angular sampling interval, to be computed for electrically large objects at microwave frequencies. Run-times of hours or less, on computing workstations or small clusters make the generation of these datasets feasible. This approach allows target fluctuation models used in subsequent radar-range-equation based calculations to be made

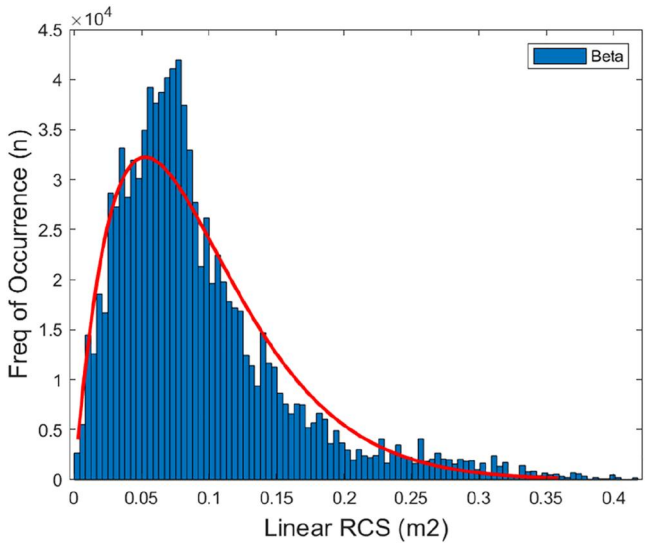


**FIGURE 34** 1.3 GHz RCS distribution, HH pol'n, broadside, s. d. = 10°, Beta dist'n applied.

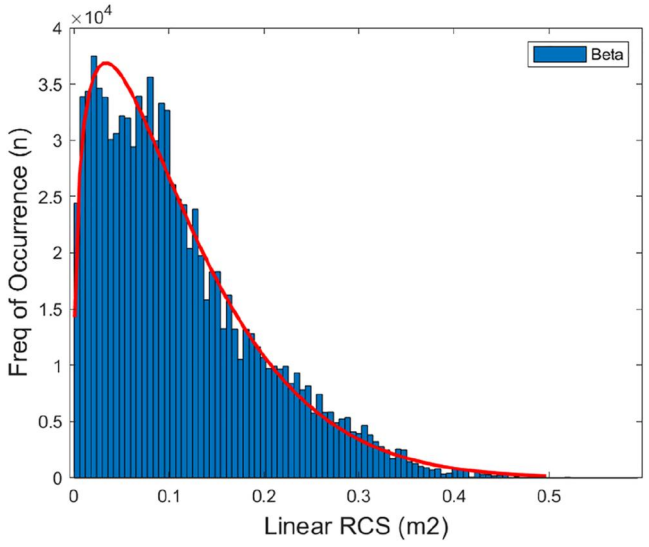


**FIGURE 35** 3 GHz RCS distribution, HH pol'n, broadside, s. d. = 10°, Beta dist'n applied.

specific to particular target cases. One could thus develop a custom fluctuation model for a particular target geometry, polarisation case, nominal viewing angle, and angular sampling, over a radar's 'dwell' period. This then offers an alternative approach to the adoption of the traditional Swerling models, albeit at the cost of having to develop custom single-pulse $P_d$ versus SNR curves for a given $P_{fa}$. A method to do this is given in ref. [5], starting with computation of the shape and scale factors for the fitted PDF.

In the HF and VHF bands, where the target is arguably a semi-Rayleigh scatterer, results suggest that the Swerling I/II and III/IV distributions that are generally applicable for typical targets at microwave frequencies are not likely to adequately

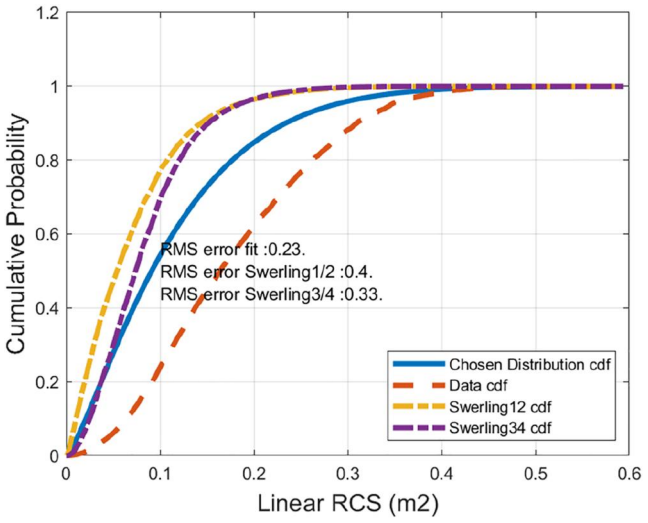


**FIGURE 36** CDF's and RMS errors for the three fits.

represent fluctuations of HGV targets at these lower frequencies. In the case chosen, the low frequency results are perhaps best assumed either to be Swerling 0 (i.e. fluctuation invariant), or, where extra accuracy is required, by a discontinuous PDF based on a Kernel or similar distribution type.

At UHF and microwave frequencies, Gamma and Beta distributions were found to represent the data well, typically better than the ubiquitous Swerling models. The exponential and Chi-squared distributions postulated by Swerling are special cases of the Gamma distribution and so it is perhaps not too surprising that the more generalised Gamma represents a good fit to this and other datasets in the higher frequency bands.

Only one particular sampling case has been presented, albeit across a range of frequency bands. However, the *Matlab* routine, as written, allows many other nominal look angles, sampling distributions, angular sampling ranges and polarisations to be explored in terms of their impact on any resultant PDF used to represent target fluctuations. This data can be used in radar-range-equation-based calculations to improve the accuracy of the SNR and so $P_d$ and maximum detection range estimates.

## AUTHOR CONTRIBUTIONS

**Jonathan Pinto**: Writing—original draft; software (lead); methodology (lead). **Neil L. Whyman**: Funding acquisition; writing—review and editing (equal). **Matthew A. Ritchie**: Supervision (equal); writing - review and editing (equal), **Hugh Griffiths**: Supervision (lead).

## ACKNOWLEDGEMENTS

This work was funded by the BAE Systems from internal research budgets.

## CONFLICT OF INTEREST STATEMENT

No conflicts of interest have been identified.

## DATA AVAILABILITY STATEMENT

Research data are not shared.

## ORCID

*Jonathan Pinto* https://orcid.org/0009-0008-3228-4825
*Matthew A. Ritchie* https://orcid.org/0000-0001-8423-8064
*Hugh Griffiths* https://orcid.org/0000-0002-9947-5553

## REFERENCES

1. Swerling, P.: Probability of Detection for Fluctuating Targets. USAF Project, RAND Research Memorandum, RM-1217 (1954)
2. Marcum, J.I.: A Statistical Theory of Target Detection by Pulsed Radar. The RAND Corporation, Research Memorandum RM-7 (1947)
3. Chaumette, E., Larzabal, P.: Monopulse-radar tracking of swerling III-IV targets using multiple observations. IEEE Trans. Aero. Electron. Syst. 44(No.2), 520–537 (2008). https://doi.org/10.1109/taes.2008.4560204
4. Backes, T., Donnie Smith, L.: Improved RCS Model for Censored Swerling III and IV Target Models IEEEAC Paper #2812, Version 5, 29/01/13
5. Pinto, J., et al.: Representation of hypersonic glide vehicles and fluctuating radar targets. In: Intl Conf. on Radar Systems. Edinburgh (2022). E-ISBN : 978-1-83953-777-6
6. Encyclopaedia Britannica Article: Strategic Missiles. https://www.britannica.com/technology/rocket-and-missile-system/Strategic-missiles#ref57333-. Accessed 6 April 2022
7. Wikipedia Article: List of Missiles. https://en.wikipedia.org/wiki/List_of_missiles. Accessed 23 March 2022
8. Military Today Article: DF-17. http://www.military-today.com/missiles/df_17.htm. Accessed 23 March 2022
9. BBC News Article: Russia Deploys Avangard Hypersonic Missile System. https://www.bbc.co.uk/news/world-europe-50927648. Accessed 23 March 2022
10. Aerosociety News Article: From Sanger to Avangard – Hypersonic Weapons Come of Age. https://www.aerosociety.com/news/from-saenger-to-avangard-hypersonic-weapons-come-of-age/. Accessed 11 March 2022
11. Missile Threat Article: RS-28 Sarmat. https://missilethreat.csis.org/missile/rs-28-sarmat/. Accessed 6 April 2022
12. Wikipedia Article: Trident (Missile). https://en.wikipedia.org/wiki/Trident_(missile). Accessed 11 March 2022
13. United Nations Office for Disarmament Affairs: ATSMUN2018, pdf Document on The Intercontinental Ballistic Missile – Antoniou T. https://www.atsmun.gr/wp-content/uploads/2018/02/DISEC_Ballistic-Missiles.pdf. Accessed 23/06/2023.10
14. Gona, S., Thomasek, P., Kresalek, V.: Measurement of conductivity of carbon fibers at microwave frequencies. In: 23rd Conf. Radioelektronica (2013). 978-1-4673-5517-9 ©2013
15. Lord, J.: User Manual for the FDTD Software 'AGATE"', Issue 4, Ref. 217/TNT/014, Issue G
16. Nayak, S.K., Thomas, M.J.: Electrical characterisation of airborne vehicle exhaust plume. IEEE Trans. Dielectr. Electr. Insul. 16(No.2), 325–334 (2009). https://doi.org/10.1109/tdei.2009.4815160
17. Knott, E.F., Schaeffer, J.F., Tuley, M.T.: Radar Cross Section. 1 Ed. Artech House (1985). ISBN : 0-89006-174-2.52 et seq
18. Pinto, J., et al.: Scale Model RCS – EM Prediction Codes versus Measurements", BAE Systems Internal Report (2018). GSE/180031/123360
19. Principles of Synthetic Aperture Radar, https://topex.ucsd.edu/rs/sar_summary.pdf, retrieved 20/06/2023
20. Randrianandrasana, M.E., Randriamitantsoa, P.A., Randriamitantsoa, A. A.: Radar cross section (RCS). IJARIEE 8(Issue-3) (2022). (IJARIIE-ISSN(O)-2395-4396)
21. Ruck, G.T.: Radar Cross Section Handbook. Plenum Press (1970)
22. Skolnik, M.C.: The Radar Handbook, Section 2.21 et seq. 2 Ed. McGraw-Hill (1989). ISBN-10:007057913X

**How to cite this article:** Pinto, J., et al.: Statistical analysis of hypersonic glide vehicle radar cross section. IET Radar Sonar Navig. 1–13 (2023). https://doi.org/10.1049/rsn2.12432